HiSST: 2nd International Conference on
High-Speed Vehicle Science & Technology
12–15 September 2022, Bruges, Belgium

Transpiration Cooling of Hypersonic Flow Past a Flat Plate with Porous Injection

Pushpender K. Sharma[1], Ralf Deiterding[2], Neil Sandham[3]

Abstract

The strategy of transpiration-based cooling is explored where the coolant is injected into the hypersonic cross-flow using a porous layer, providing a gradual and more uniform distribution of the coolant into the boundary layer and hence higher effectiveness. In the present numerical study, three-dimensional direct numerical simulations of flow past a flat plate with a porous layer are conducted at $M = 5$. A conjugate heat flux boundary condition is used as compared to a simpler isothermal wall. The coolant is injected through a porous layer that is numerically represented as a staggered arrangement of spheres, which requires the utilization of smaller pressure ratios similar to that in the corresponding actual experiments. Also, to mimic the background disturbances intrinsic to the experiments, wall-bounded disturbances are introduced upstream of the porous layer such that reasonable mixing of coolant is allowed inside the hypersonic boundary layer. Flow transition is noted to play a critical role in the performance. It is noted from the first set of moderately high injection Reynolds number cases that the lowest blowing ratio results in more cooling immediately downstream of the porous layer, while the highest blowing ratio shows overall best results, with highest cooling effectiveness even farther downstream among all the blowing cases. For the second set of slightly higher injection Reynolds number cases, the trend is much more monotonous, with increasing blowing ratios providing increasingly better effectiveness.

Keywords: *High-speed compressible flows, transpiration cooling, porous layer, transitional flows*

Nomenclature

Latin

A – Amplitude of disturbance
PR – Pressure ratio
BR – Blowing ratio
Re_u – unit Reynolds number (1/m)
Re_{inj} – Reynolds number at injection location
x – Distance from computational inflow plane
$\tilde{x}$ – Distance from flat plate leading edge

Greek

δ^* – Displacement thickness at inflow plane
ω_0 – Frequency of excitation
β_0 – Spanwise wavenumber of excitation
α_0 – Streamwise wavenumber of excitation

Superscripts

$*$ – Dimensional quantity

Subscripts

inj – Injection location

1. Introduction

There is a renewed interest in recent times for alternate methods of effectively cooling the surface of high-speed vehicles, such as the injection of coolant into the flow stream. The active cooling methods have applications where the re-usability of thermal protection systems (TPS) is important. Various coolant injection techniques [1, 2] have been explored, as the vehicles at hypersonic speeds experience very high surface heat fluxes. In general, the active cooling methods can be categorised into three categories: convective cooling, film/effusion cooling, and transpiration cooling [3]. Primarily two main

[1]*Research Fellow, Aerodynamics & Flight Mechanics Group, University of Southampton, Southampton SO16 7QF, United Kingdom, p.k.sharma@soton.ac.uk*
[2]*Professor, Aerodynamics & Flight Mechanics Group, University of Southampton, Southampton SO16 7QF, United Kingdom, r.deiterding@soton.ac.uk*
[3]*Professor, Aerodynamics & Flight Mechanics Group, University of Southampton, Southampton SO16 7QF, United Kingdom, n.sandham@soton.ac.uk*

techniques of active cooling are explored by the researchers, namely, a) effusion cooling [4, 5, 6, 7], where the coolant injection occurs through localised holes/slots, and b) transpiration cooling [2, 8, 9], in which coolant transpires more uniformly through the surface of a porous material. The transpiration cooling methods are regarded as more efficient thanks to the enhanced heat exchange between coolant and structure with multiple pores of micrometer dimension [2, 10]. The coolant passes through the porous layer and then forms a thin film on top of the porous layer as it exits the porous layer, whereas effusion through holes/slots may cause early transition due to the impinging jets, hence reducing the laminar extension of the boundary layer. This suggests a need to further explore the benefits of using transpiration-based cooling systems. Direct numerical simulations (DNS) are a very useful tool to do such studies, especially as these have the capability to capture the small-scale flow details, which are otherwise difficult to measure experimentally. There have been a few DNS studies looking at the transpiration cooling methods [11, 12], but not many are available at hypersonic speeds. Hence, the present study aims at providing detailed insight into the transpiration cooling at hypersonic speeds using various coolant blowing ratios to inject the coolant into the hypersonic flow through an artificial porous sample. The complex structure of the porous material used in transpiration cooling experiments is hard to represent numerically, and hence a simplified arrangement of spheres is used, which mimics the behaviour of real porous material in terms of the blowing ratio and mass flux.

2. Solver details

The solver used is a in-house parallel solver, called AMROC (Adaptive Mesh Refinement using Object Oriented C++) [13]. It is a finite-volume-based solver with parallel structured adaptive mesh refinement (SAMR) capability. This allows for higher resolution in the small pore length scales of the porous layer. The system of 3D dimensionless governing equations for compressible Navier-Stokes equations are solved in conservation form, under the assumption of constant specific heats, along with the species conservation equation to track the coolant concentration (or mass fraction, Y_1) in the flow [10]. A hybrid WENO-CD scheme is used for inviscid fluxes, i.e., a 6^{th}-order central differencing (CD) scheme in space for smooth regions, combined with a 6^{th}-order weighted-essentially-non-oscillatory (WENO) scheme for shock capturing [14, 15, 10]. Viscous fluxes calculation is also done using a sixth order CD scheme in space, and a 3^{rd}-order Runge-Kutta method is used for time integration.

3. Numerical set-up

The numerical set-up used here corresponds to the experiments performed in the high-density tunnel at the Oxford Thermofluids Institute, using an ultra-high temperature ceramic (UHTC) as porous material [9]. A 2D schematic showing the side view of the experimental set-up along with the computational set-up marked by red dashed lines is depicted in Fig. 1. The free-stream conditions are M=5, T^*_∞=76.66 K, ρ^*_∞=0.07979 Kg/m^3 and p^*_∞=1.75×10^3 Pa, which results in a unit Reynolds number (Re_u) of 12.6×10^6 (1/m). The experimental set-up consists of a flat plate with a sharp leading edge, while the inflow plane of the computational domain is constructed at a certain distance downstream of the leading edge using a laminar boundary layer similarity solution to reduce the computational expense by computing in a smaller domain. The inflow plane of the computational domain (at x=0) is located approximately at $\tilde{x}^*_0$=127 mm from the leading edge of the flat plate, such that the displacement thickness of the boundary layer at the inflow plane is δ^*=1 mm. This δ^*=1 mm is also used as the characteristic length scale and therefore all the lengths are scaled with a length of 1 mm. A characteristic Reynolds number of $Re_{\delta^*} = Re_u\delta^*$=12600 is obtained based on δ^*=1 mm, and is imposed in the simulations.

The computation domain, marked as red dashed lines in Fig. 1, is a 3D rectangular box with periodicity in the spanwise (z) direction and is initialized using the compressible Blasius similarity solution, which constructs a spatially growing boundary layer with the streamwise length of the domain. The non-dimensional extents of the domain in x-, y-, and z-directions are 0 to 160, -1.28 to 22.72, and -4 to 4, respectively. A grid with $N_x \times N_y \times N_z = 2000 \times 300 \times 100$ cells is used for the coarsest level. As the solver has SAMR capability, two levels of grid refinement are used to ensure enough resolution in the porous layer region and very close to the wall, as shown in Fig 2. It takes about 48,000 CPU-hours to reach a non-dimensional time of $t = t^*/(\delta^*/U_\infty) \approx 500$, (or dimensional time t^*=0.569 ms) using 400 processor cores. The smooth flat plate is placed at $y = 0$, and a porous layer sample of length (streamwise),

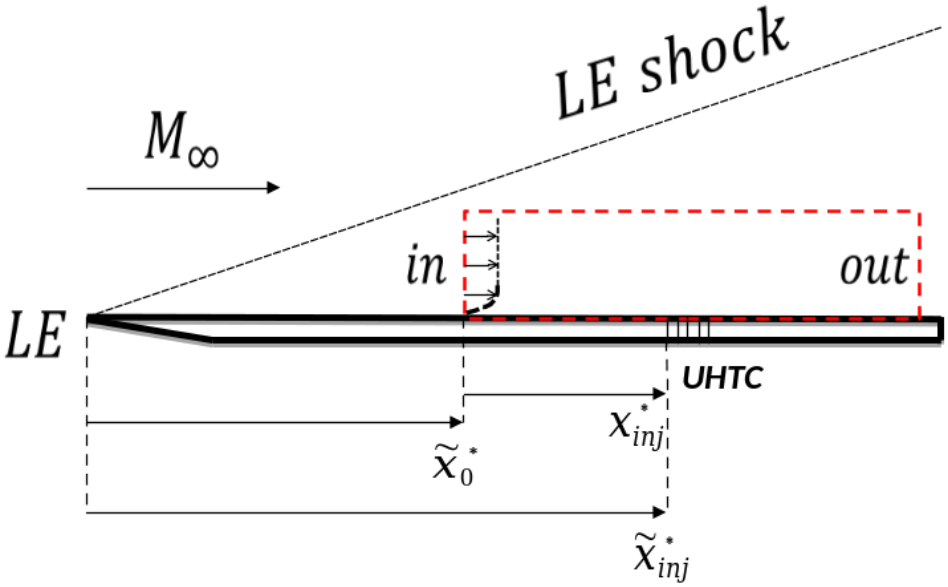

Fig 1. A 2D schematic showing full experimental set-up with the leading edge, while the smaller computational domain is marked as red dashed line. The porous-layer, marked as UHTC, is placed at x^*_{inj} from the computational inflow plane or at $\tilde{x}^*_{inj}$ from the leading edge of the flat plate. The computational inflow plane is at $\tilde{x}^*_0 \approx 127$ mm from the leading edge.

width (spanwise) and height (wall-normal) as 39 $\times$ 8 $\times$ -1.28 is placed for the first set of cases between $x = 35$ and $x = 74$, and the second set of cases between $x = 46$ and $x = 85$. For the first set of cases, the starting location of the porous layer is at $x_{inj,1} = 35$ from the computation inflow plane, or at $\tilde{x}_{inj} = 127 + 35 = 162$ or $\tilde{x}^*_{inj} = 162$ mm from the sharp leading edge. This determines the Reynolds number at the injection location, i.e., $R_{inj,1} = Re_u \tilde{x}^*_{inj} = 2.04 \times 10^6$. Similarly, for the second set of cases, where $x_{inj,2} = 46$, another injection Reynolds number of $R_{inj,2} = 2.18 \times 10^6$ is obtained. These two significantly high injection Reynolds numbers, $R_{inj,1}$ and $R_{inj,2}$, are chosen because a significant difference in the wall heat flux values was noted in the experiments [9].

In the simulations, an artificial porous layer is created with a staggered arrangement of spheres with a body-centered cubic (BCC) packing and is used to blow the coolant uniformly into the oncoming hypersonic cross-flow. Various pressure ratios (PR) are considered and are chosen such that similar blowing ratios (BR) as observed in the experiments are obtained numerically, hence maintaining same coolant mass efflux, as shown in Tables 1 and 2. The blowing-suction disturbances of the form, $v'(x, z, t) = A \cos(\beta_0 z) \cos[\alpha_0(x - x_0) - \omega_0 t]$ are imposed in the v-component of the velocity at $y = 0$ between $x = 10$ to 30 to perturb the flow and introduce uniform mixing of the coolant downstream. Here, A is the amplitude and $\beta_0 = 2\pi/\lambda_z$ is the non-dimensional spanwise wavenumber with a spanwise wavelength of $\lambda_z = 8/3$, and $\alpha_0 = 2\pi/\lambda_x$ is the streamwise wavenumber with $\lambda_x = (30 - 10) = 20$ as streamwise wavelength. Also, the disturbances start at $x_0 = 10$, and a non-dimensional frequency of $\omega_0 = 0.162$ is used. These modes are identified in an earlier linear stability study shown in [16, 17]. More realistic conjugate heat flux (CHF) boundary conditions are applied at the wall compared to a simpler isothermal wall, where heat fluxes from the fluid and solid side are equated to obtain the surface temperature.

4. Results

As mentioned in the previous section, two sets of fairly high injection Reynolds numbers are studied in detail. The first set of cases is simulated for injection Reynolds number, $R_{inj,1} = 2.04 \times 10^6$, where the leading edge of the porous sample is placed at $x_{inj,1} = 35$, and are reported in Table 1, showing all the 3D numerical simulations performed for this injection Reynolds number with and without blowing.

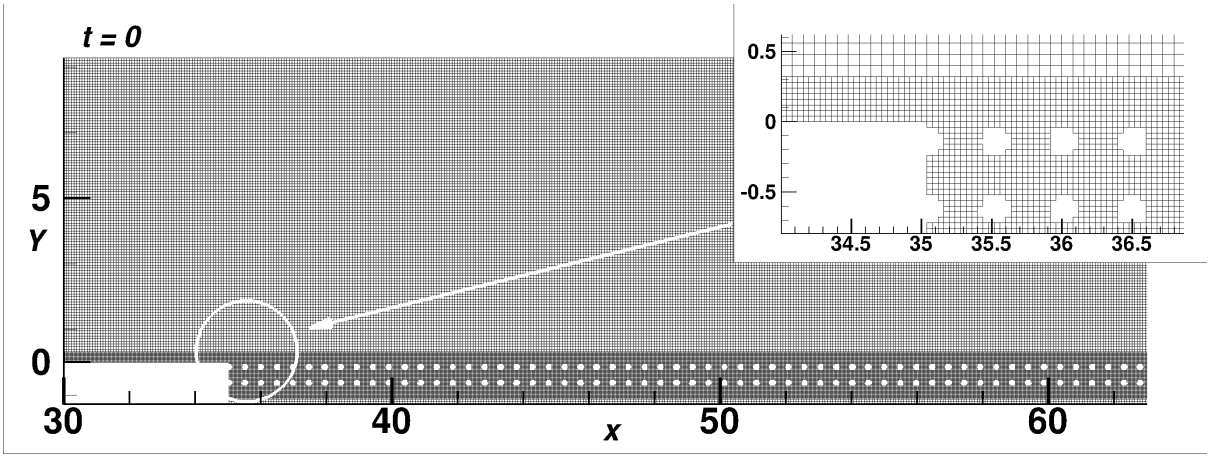

Fig 2. Two levels of mesh are shown at $t = 0$ at an x-y plane at $z = -0.001$, while a zoomed view near the porous layer leading edge is shown in the inset. The 2D cut section of the 3D porous layer only captures the top and bottom rows of spheres, and does not show the third intermediate layer of spheres in the figure.

The second set of results is for $R_{inj,2} = 2.18 \times 10^6$, where the leading edge of the porous sample is placed at $x_{inj,2} = 46$, and the 3D numerical simulations corresponding to this are reported in Table 2. As mentioned in the previous section, the porous sample is composed of staggered layers of spheres in a BCC packing and is placed inside the plenum chamber of depth 1.5 mm. The thickness of the porous layer is approximately 0.7 mm, as can be seen from Fig. 2. In the figure, only two layers of the spheres can be discerned, while the intermediate layer can not be seen due to the placement of the cut-section at the maximum diameter of the first and third row of spheres. Various pressure ratios are used in the simulations, which are implemented by constantly imposing a higher pressure at the bottom of the plenum chamber at $y = -1.5$ through the boundary condition. The plenum is also initialised with higher pressure below the sphere layer, while the pressure decreases linearly through the porous layer all the way to the free-stream pressure at $y = 0$.

Table 1. Cases considered for $Re_{inj,1} = 2.04 \times 10^6$

Case No.	*PR*	*BR*	Disturbance Amplitude
1a	1	0	5%
2a	1.15	0.0020	5%
3a	1.3	0.0030	5%
4a	1.5	0.0065	5%

Table 2. Cases considered for $Re_{inj,2} = 2.18 \times 10^6$

Case No.	*PR*	*BR*	Disturbance Amplitude
1b	1	0	10%
2b	1.15	0.0020	10%
3b	1.3	0.0060	10%
4b	1.4	0.0080	10%

These different pressure ratios result in the various blowing ratios of the coolant at the exit of the porous layer, and a typical blowing ratio plot is shown in Fig. 3 for $R_{inj,1}$ cases corresponding to different

pressure ratios. As noted from the figure, a nearly homogeneous injection of coolant is created with the help of the sphere arrangement. The blowing ratio is largely uniform over the porous sample length, showing significant increase only towards the end of the porous sample. This increase is happening as the pressure starts to recover back to the free-stream value towards the end of the porous sample.

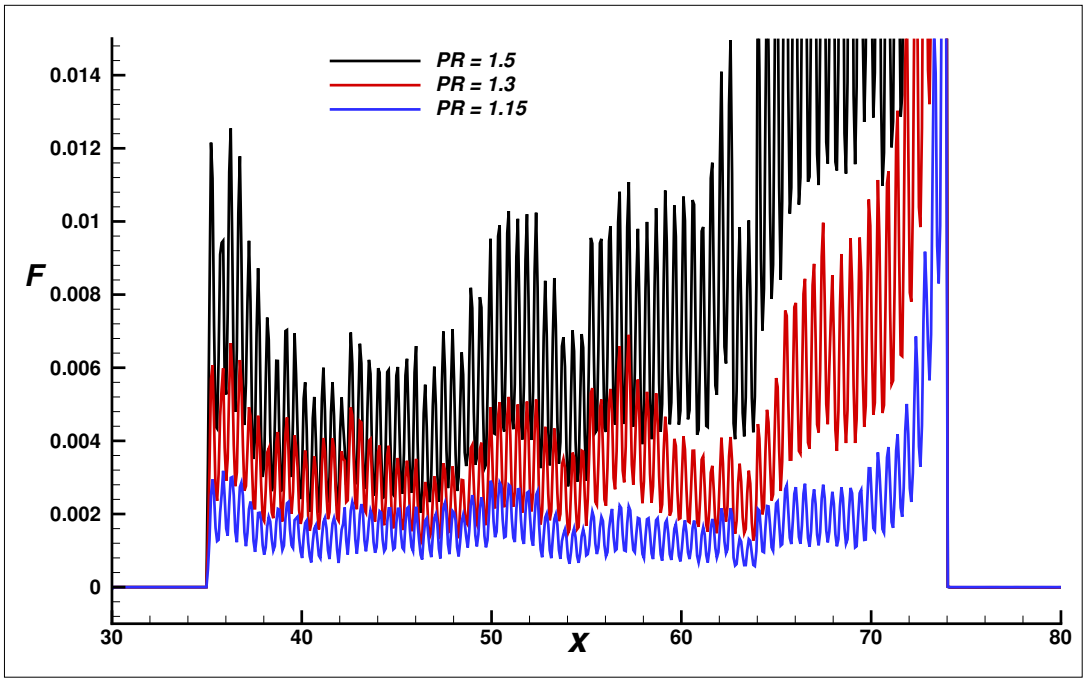

Fig 3. Span-time averaged values of blowing ratio ($BR = F = \rho v$) at the exit of the porous layer at $y = 0$.

Case-1a and Case-1b in Tables 1 and 2 correspond to the no-blowing cases for $Re_{inj,1}$ and $Re_{inj,2}$, respectively, which are the base/reference cases without any coolant injection. It is noted from the experiments that the no-blowing cases themselves are transitional. This requires perturbing the flow in the computational set-up such that similar wall heat flux values are obtained numerically, as noted in the experiments. For these no-blowing cases, the transition is visually observed to be happening after the porous sample for the first injection Reynolds number, $Re_{inj,1}$, while it occurs over the porous sample itself in the case of the higher injection Reynolds number, $Re_{inj,2}$. To achieve this, the wall bounded perturbation of amplitude $A = 5\%$ is used for the $Re_{inj,1}$ cases, while amplitude of $A = 10\%$ is required for $Re_{inj,2}$ cases. This is demonstrated using Fig. 4, which shows the boundary layer demarcated by $u-$component of velocity cut off at 0.99 of the free-stream value. The boundary layer is noted to undergo transition after the porous sample for Case-1a of $Re_{inj,1}$, while it is clearly transitioning over the porous sample itself for Case-1b of $Re_{inj,2}$.

The various cases, with and without blowing, simulated in the present study are listed in Table 1 and Table 2, for two injection Reynolds numbers, i.e., $Re_{inj,1} = 2.04 \times 10^6$ and $Re_{inj,2} = 2.18 \times 10^6$, respectively. The detailed discussion of the results for these are presented next.

4.0.1. Results for $Re_{inj,1} = 2.04 \times 10^6$ with porous sample at $x = 35$

First, results with respect to $Re_{inj,1}$ are discussed. A 3D picture representative of the flow field is shown in Fig. 5 for Case-2a from Table 1, where the coolant concentration (Y_1) is shown at an x-z plane at $y = 0.1$ and multiple y-z planes at various streamwise locations, while the u-component of velocity is shown on an x-y plane at $z = -4$. Here, coolant concentration (Y_1) is nothing but the mass fraction of coolant in the mixture. The figure is plotted starting from a streamwise distance of $x = 50$, showing only a part of the porous sample which is between $x = 35$ and $x = 74$. A higher coolant concentration is noted on the x-y plane above the porous layer, while it decreases as one moves downstream. As

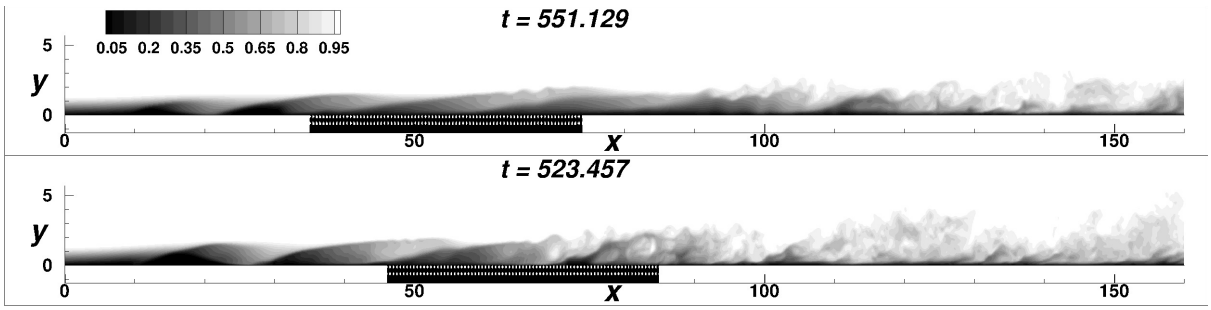

Fig 4. u-component of velocity at an x-y plane at $z = -0.001$ for no-blowing cases, i.e., Case-1a of $Re_{inj,1} = 2.04 \times 10^6$ (top frame) and Case-1b of $Re_{inj,2} = 2.18 \times 10^6$ (bottom frame).

the boundary layer, shown through the u-velocity component on the side plane at $z = -4$, transitions to turbulence around $x \approx 100$, the coolant also starts to get mixed within the boundary layer. This mixing leads to a distribution of coolant and diffuses it away from the wall, as seen from the y-z planes downstream of $x \approx 100$, degrading the cooling performance further on. Upstream of the transition location, the flow forms a thin coolant film close to the wall for this lowest blowing ratio case (Case-2a), resulting in lower wall heat flux values and higher effectiveness.

Similarly, to get an idea of what's happening at a higher pressure/ blowing ratio, Fig. 6 is plotted for Case-4a. As this case has the highest blowing ratio among cases in Table 1, it results in an early transition of the flow starting over the porous sample itself, as seen from the side plane at $z = -4$. The higher blowing ratio also leads to the thickening of the boundary layer compared to the lowest blowing ratio Case-2a, as noted from the side planes at $z = -4$. Although transition occurs earlier in Case-4a, a higher coolant concentration is noted over and downstream of the porous sample. This results in much better performance over a large region downstream of the porous sample, as seen in the wall heat flux values shown next.

After having looked at the qualitative picture of the flow field, a quantitative picture of the flow field is shown in Fig. 7, comparing span and time averaged wall heat flux values among various cases for $Re_{inj,1}$. The wall heat flux values are plotted downstream of the trailing edge of the porous layer starting at $x = 74$ to look at the cooling performance downstream. It can be noted from Fig. 7 that the lowest $PR = 1.15$ case, i.e., Case-2a, with the lowest blowing ratio, shows the lowest heat flux values immediately downstream of the porous layer till $x \approx 110$, but once the transition is triggered, the wall heat flux values deteriorate and reach values similar to the no-blowing case. The intermediate $PR = 1.3$ case, i.e., Case-3a, shows the highest values of heat fluxes among all blowing cases in the vicinity and even downstream of the porous layer. However, it can be seen that the case with the highest pressure of $PR = 1.5$, i.e., Case-4a, gives the best cooling effectiveness over a longer stretch of flat plate downstream of the porous layer.

The explanation for this behaviour is that the highest blowing ratio leads to higher mixing of the coolant within the boundary layer, and as the coolant content due to the highest blowing ratio of $BR = 0.0065$ is also highest for Case-4a among all cases, higher cooling is noted for this case starting from the trailing edge of the porous layer at $x = 74$ and also shows lowest heat flux values after $x \approx 110$ among all the presented cases. For the intermediate case of $PR = 1.3$, i.e., Case-3a, although the mixing does start early, the coolant content ($BR = 0.0030$) is far less compared to the $PR = 1.5$ case, and hence very high heat flux values are noted for Case-3a, even worse than the no-blowing Case-1a. For the lowest $PR = 1.15$ case, the coolant forms a film immediately downstream of the porous layer up to $x \approx 100$ and then starts to transition, showing very high heat fluxes almost equal to that of Case-3a. A similar performance can also be noted from the corresponding plots in the bottom frame in Fig. 7 for the cooling effectiveness, $\eta = (1 - q_{w,c}/q_{w,nc})$, where $q_{w,c}$ and $q_{w,nc}$ are the wall heat fluxes with and without coolant, respectively. The lowest blowing ratio case, Case-2a, shows the best effectiveness till $x \approx 110$ and then deteriorates afterwards, while the highest blowing ratio case, Case-4a, provides decent

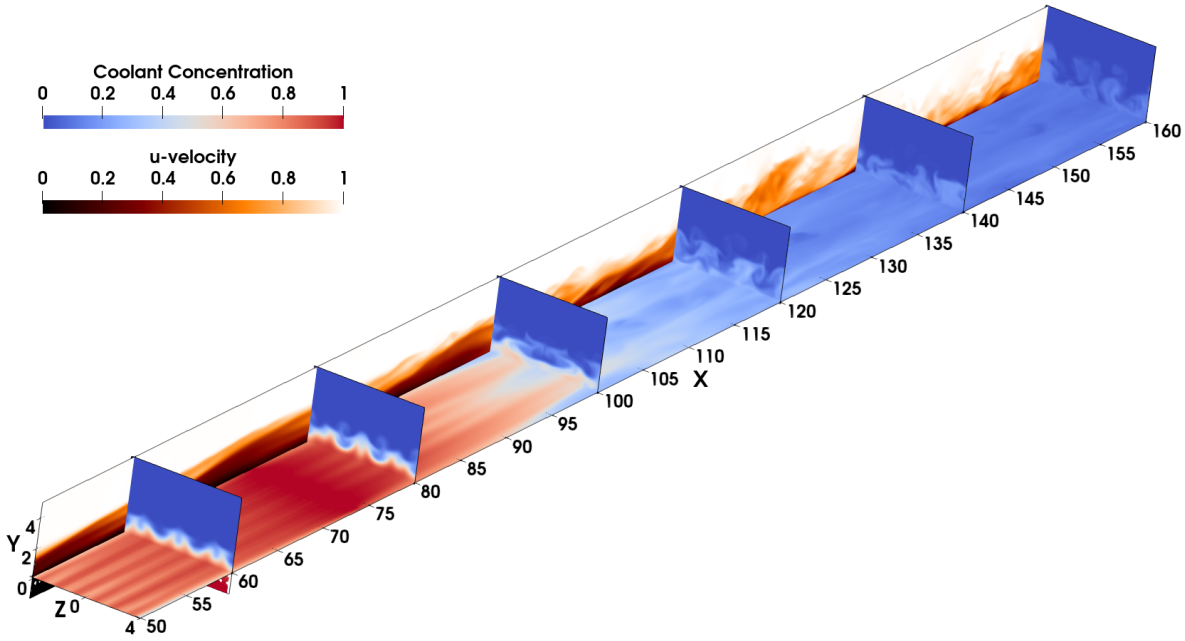

Fig 5. 3D view of flow field downstream of $x = 50$ for Case-2a at $t = 456.5$, showing a) coolant concentration on x-z plane at $y = 0.1$ and on multiple y-z planes along x-direction, b) u-velocity component on x-y plane at $z = -4$.

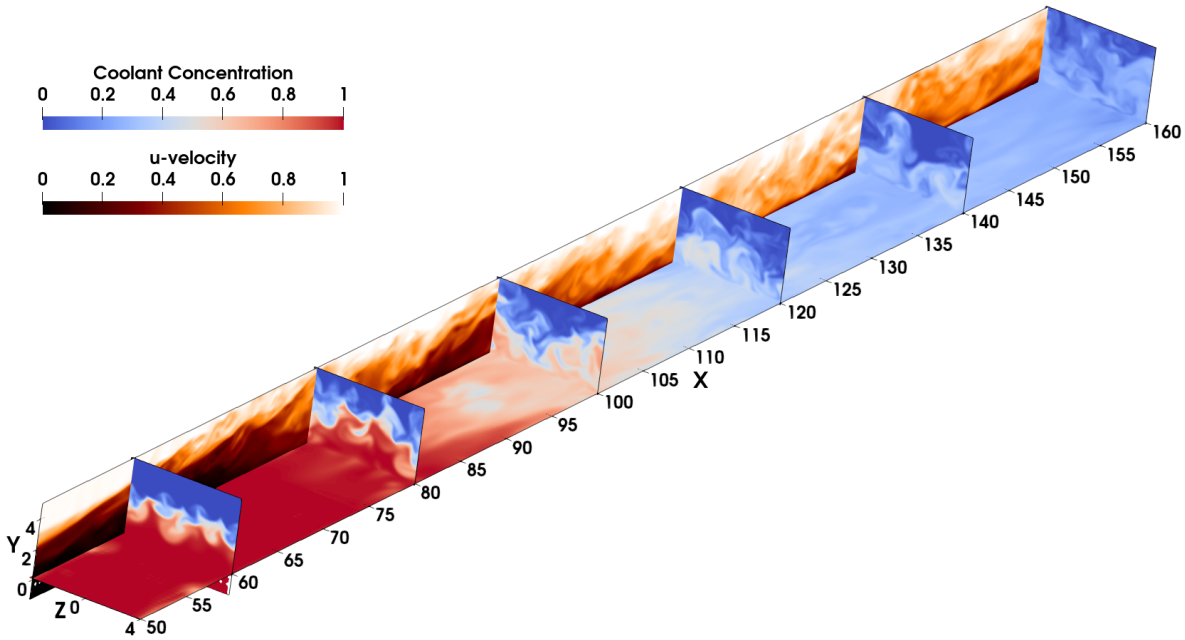

Fig 6. 3D view of flow field downstream of $x = 50$ for Case-4a at $t = 462.69$, showing a) coolant concentration on x-z plane at $y = 0.1$ and on multiple y-z planes along x-direction, b) u-velocity component on x-y plane at $z = -4$.

effectiveness till $x \approx 110$ and shows the best effectiveness among all blowing cases afterwards.

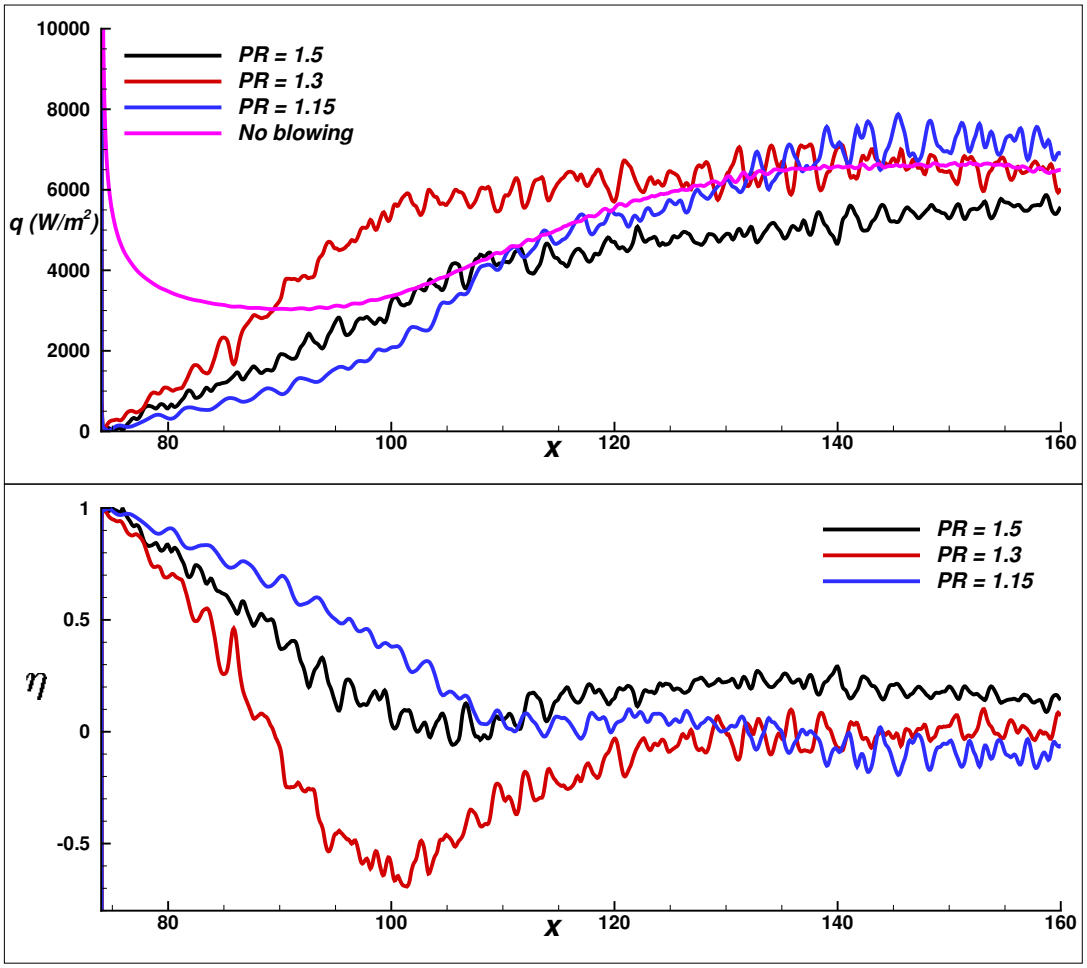

Fig 7. Wall heat fluxes for different pressure ratio (PR) cases (top frame) and cooling effectiveness (bottom frame), starting from the trailing edge of the porous layer at $x = 74$.

Figure 8 further shows the coolant concentration at a plane close to mid-span location at $z = -0.001$. This figure further validates the wall heat flux results noted in Fig. 7. It can be seen from the bottom-most frame in the figure for Case-2a at a later time that there is indeed a coolant film that forms downstream of the porous layer till approximately $x \approx 100$ and starts to transition to turbulent flow afterwards. Furthermore, as one moves from the bottom frame towards the middle and the top frame, the transition location keeps moving backwards, occurring after the middle of the porous sample for Case-3a, while it starts almost near the leading edge of the porous sample for Case-4a. This is also shown through boundary layer plots in Fig. 9 for the corresponding cases at the same times as shown in Fig. 8. It can be noted that the coolant starts to mix around the same streamwise location where the boundary layer is noted to undergo transition. Boundary layer transition is noticed around $x \approx 110$ for Case-2a in the bottom frame, while the middle frame shows transition post the midsection and towards the end of porous sample for Case-3a in the middle frame. For Case-4a, the boundary layer is already transitional over the porous sample starting from the leading section itself.

4.0.2. Results for $Re_{inj,2} = 2.18 \times 10^6$ with porous sample at $x = 46$

In this section, results corresponding to the second injection Reynolds number, $Re_{inj,2} = 2.18 \times 10^6$, are presented, where the leading edge of the porous sample is placed at $x = 46$. Again, four cases are considered and are listed in Table 2. Also, as mentioned earlier and shown in Fig. 4, the transition for the no-blowing case, Case-1b, starts over the porous sample itself for $Re_{inj,2}$. This results in much

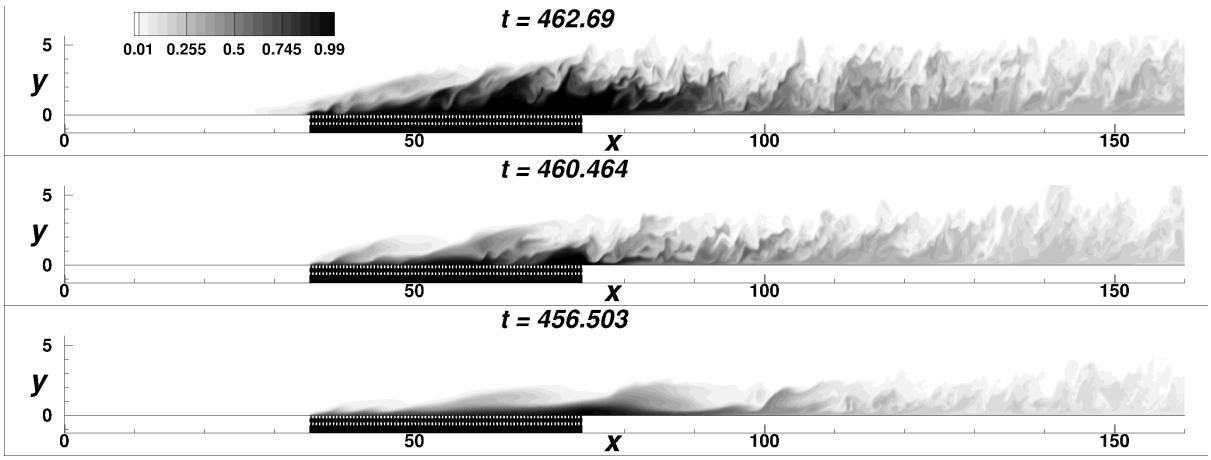

Fig 8. Coolant concentration (Y_1) shown for the three blowing cases at exact same x-y plane at $z = -0.001$. Top, middle, and bottom frames show Case-4a, Case-3a, and Case-2a, respectively.

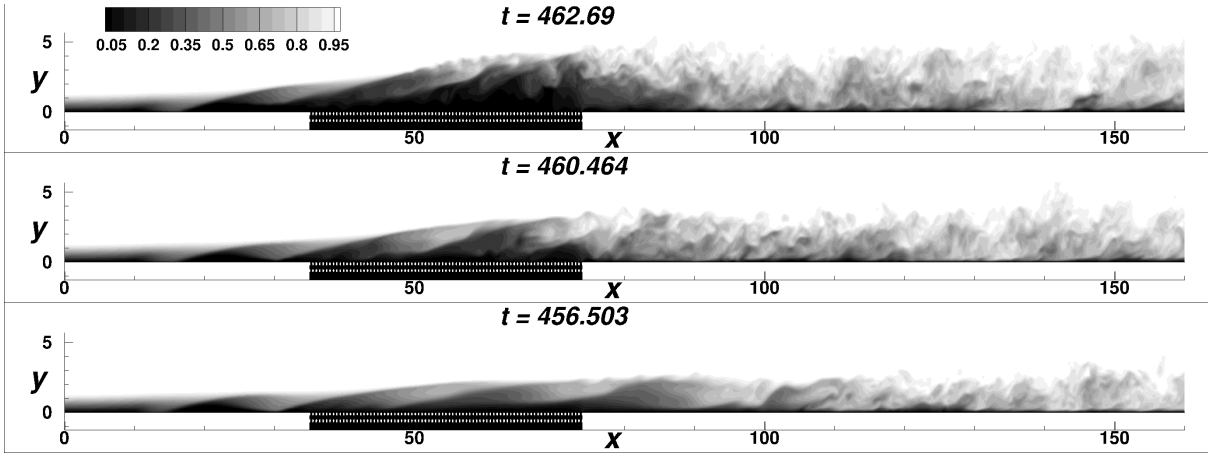

Fig 9. u-component of velocity shown for the three PR cases. Top, middle, and bottom frames show Case-4a, Case-3a, and Case-2a, respectively.

higher heat flux values as seen from Fig. 10 downstream of the trailing edge of the porous sample that is located between $x = 46$ and $x = 85$. These values are much higher than those observed in the case of $Re_{inj,1}$, especially when comparing the no-blowing cases. Interestingly, in the $Re_{inj,2}$ cases, a monotonic decrease in the heat flux values is noted with the injection of the coolant in the flow. The no-blowing case results in the highest heat flux values, while the cases with increasing pressure/ blowing ratios show a monotonous decrease. While the lowest blowing ratio case, Case-2b, does not provide a significant drop in heat flux values, the higher blowing ratio cases, i.e., Case-3b and Case-4b, provide a significant drop, with Case-4b showing the best results in terms of the wall heat flux and cooling effectiveness as can be inferred from Fig. 10.

Figure 11 also looks at the physics in terms of the coolant concentration for the blowing cases, showing Case-2b, Case-3b, and Case-4b in the bottom, middle, and top frames, respectively. The boundary layer is transitional over the porous sample for the no-blowing case itself, and hence, the lowest blowing ratio case is also seen to be transitional over the porous sample itself. With the increase in the blowing ratio, a significantly higher coolant concentration over and downstream of the porous layer is observed, which results in a significant drop in the wall heat flux values downstream of the porous layer due to the presence of higher coolant content.

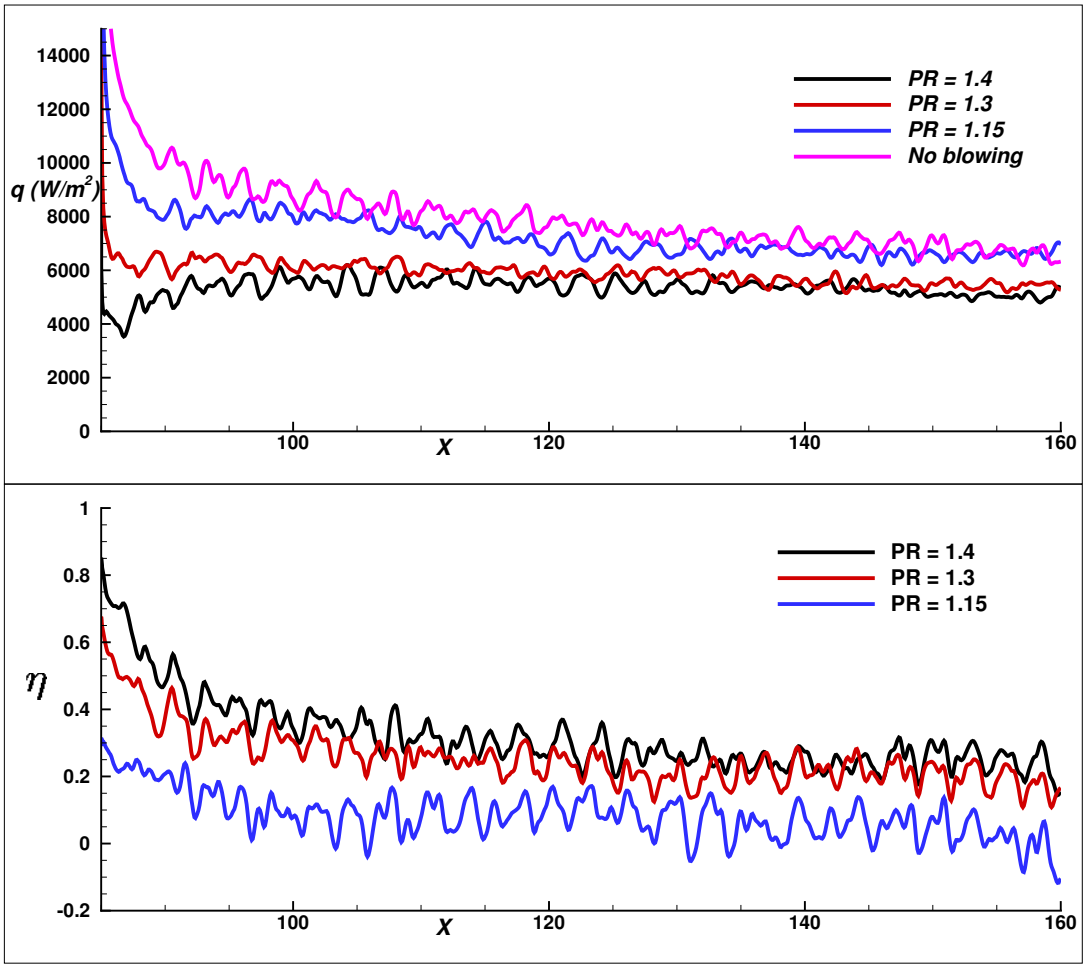

Fig 10. Wall heat fluxes for different pressure ratio (PR) cases (top frame) and cooling effectiveness (bottom frame), starting from the trailing edge of the porous layer at $x = 85$.

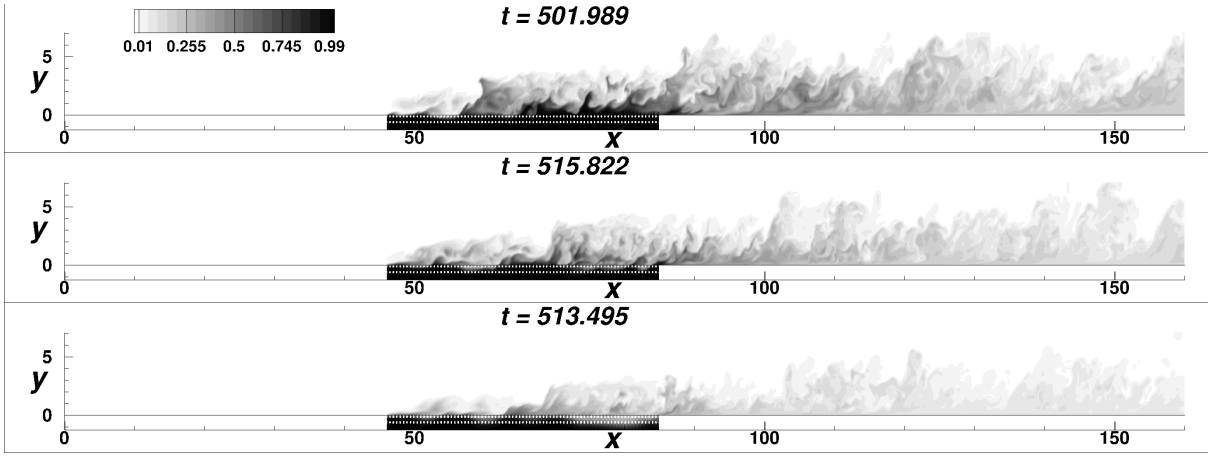

Fig 11. Coolant concentration (Y_1) shown for the three blowing cases at exact same x-y plane at $z = -0.001$. Top, middle, and bottom frames show Case-4b, Case-3b, and Case-2b, respectively.

5. Conclusions

Transpiration cooling is studied for a hypersonic flow past a flat plate at Mach number, $M = 5$. A significantly high unit Reynolds number, i.e., $Re_u = 12.6 \times 10^6$ (1/m), is considered. A porous sample, mimicked as a staggered arrangement of spheres in BCC packing, is used to represent the porous sample used in the experiments. Two different injection Reynolds numbers, i.e., $Re_{inj,1} = 2.04 \times 10^6$ and $Re_{inj,2} = 2.18 \times 10^6$, are studied with the placement of the leading edge of the porous sample in the computational domain at $x = 35$ and $x = 46$, respectively. For each of the injection Reynolds numbers, four cases with and without coolant blowing are studied. The flows are transitional in nature, and therefore, the boundary layer is appropriately perturbed using wall-bounded blowing-suction harmonic excitation to achieve flow transition as observed in the experiments for the cases without coolant blowing.

For the first injection Reynolds number, $Re_{inj,1}$, the flow transition is noted to start downstream of the porous sample. Higher heat flux values are observed for the intermediate case of $PR = 1.3$, i.e., Case-3a. The lowest pressure ratio case, Case-2a, is most effective immediately downstream of the porous layer due to the formation of coolant film; however, the performance degrades father downstream due to the triggering of flow transition, resulting in higher wall heat flux values. The highest pressure ratio case, Case-4a, not only provides good performance downstream of the porous sample but also shows the highest effectiveness farther downstream among all the blowing cases, hence giving the best results over a longer stretch downstream of the porous layer.

Higher injection Reynolds number ($Re_{inj,2} = 2.18 \times 10^6$) cases, in general, show higher heat flux values due to flow transition occurring over the porous sample itself. These cases show a very different trend compared to $Re_{inj,1} = 2.04 \times 10^6$, where the wall heat-flux values downstream of the porous layer monotonically decrease while the cooling efficiencies monotonically increase, with increasing pressure/ blowing ratios.

Therefore, from the various pressure/ blowing ratio cases for the two injection Reynolds numbers, in general, a relatively higher pressure/ blowing ratio tends to provide higher cooling effectiveness over a larger distance downstream of the porous sample and, therefore, could be used in an application scenario where multiple porous layer sections are placed slightly farther apart from each other. However, this will lead to a higher coolant consumption due to higher blowing ratios. Lower pressure/ blowing ratios may result in coolant film formation and hence provide significant effectiveness downstream of the porous sample, but only for limited scenarios.

Acknowledgments

The authors would like to acknowledge support from EPSRC (Engineering and Physical Sciences Research Council) under Grant No. EP/P000878/1. Also, we would like to acknowledge the computing resources provided by the high-performance computing center, Iridis-5, at the University of Southampton to carry out the simulations.

References

[1] A. Fitt, J. Ockendon, and T. Jones, "Aerodynamics of slot-film cooling: theory and experiment," *Journal of fluid mechanics*, vol. 160, pp. 15–27, 1985.

[2] T. Langener, J. V. Wolfersdorf, and J. Steelant, "Experimental investigations on transpiration cooling for scramjet applications using different coolants," *AIAA journal*, vol. 49, no. 7, pp. 1409–1419, 2011.

[3] M. J. Brunner, "Active cooling heat protection.," *Journal of Spacecraft and Rockets*, vol. 6, no. 6, pp. 661–666, 1969.

[4] R. Goldstein, E. Eckert, F. Tsou, and A. Haji-Sheikh, "Film cooling with air and helium injection through a rearward-facingslot into a supersonic air flow.," *AIAA journal*, vol. 4, no. 6, pp. 981–985, 1966.

[5] A. Fitt and P. Wilmott, "Slot film cooling—the effect of separation angle," *Acta mechanica*, vol. 103, no. 1-4, pp. 79–88, 1994.

[6] S. Wittig, A. Schulz, M. Gritsch, and K. A. Thole, "Transonic film-cooling investigations: effects of hole shapes and orientations," in *ASME 1996 International Gas Turbine and Aeroengine Congress and Exhibition*, pp. V004T09A026–V004T09A026, American Society of Mechanical Engineers, 1996.

[7] A. Cerminara, R. Deiterding, and N. Sandham, "Direct numerical simulation of blowing in a hypersonic boundary layer on a flat plate with slots," in *2018 Fluid Dynamics Conference*, p. 3713, 2018.

[8] J. Meinert, J-ograve, r. Huhn, E. Serbest, and O. J. Haidn, "Turbulent boundary layers with foreign gas transpiration," *Journal of Spacecraft and Rockets*, vol. 38, no. 2, pp. 191–198, 2001.

[9] T. Hermann, H. S. Ifti, M. McGilvray, L. Doherty, and R. P. Geraets, "Mixing characteristics in a hypersonic flow around a transpiration cooled flat plate model," in *HiSST: International Conference on High-Speed Vehicle Science Technology*, (Moscow, Russia), Nov. 2018.

[10] A. Cerminara, R. Deiterding, and N. Sandham, "A mesoscopic modelling approach for direct numerical simulations of transition to turbulence in hypersonic flow with transpiration cooling," *International Journal of Heat and Fluid Flow*, vol. 86, p. 108732, 2020.

[11] M. A. Keller and M. J. Kloker, "Direct numerical simulation of foreign-gas film cooling in supersonic boundary-layer flow," *AIAA Journal*, vol. 55, no. 1, pp. 99–111, 2016.

[12] N. Christopher, J. M. Peter, M. J. Kloker, and J.-P. Hickey, "Dns of turbulent flat-plate flow with transpiration cooling," *International Journal of Heat and Mass Transfer*, vol. 157, p. 119972, 2020.

[13] R. Deiterding, "Block-structured adaptive mesh refinement-theory, implementation and application," in *Esaim: Proceedings*, vol. 34, pp. 97–150, EDP Sciences, 2011.

[14] C. Pantano, R. Deiterding, D. J. Hill, and D. I. Pullin, "A low numerical dissipation patch-based adaptive mesh refinement method for large-eddy simulation of compressible flows," *Journal of Computational Physics*, vol. 221, no. 1, pp. 63–87, 2007.

[15] J. L. Ziegler, R. Deiterding, J. E. Shepherd, and D. I. Pullin, "An adaptive high-order hybrid scheme for compressive, viscous flows with detailed chemistry," *Journal of Computational Physics*, vol. 230, no. 20, pp. 7598–7630, 2011.

[16] A. Cerminara, T. Hermann, H. S. Ifti, R. Deiterding, N. Sandham, and M. McGilvray, "Influence of instability modes on cooling performance in hypersonic boundary layer with slot injection," *Aerospace Science and Technology*, vol. 109, p. 106409, 2021.

[17] A. Cerminara, R. Deiterding, and N. Sandham, "Dns of injection-induced transition in hypersonic flow over porous surfaces for transpiration cooling applications," in *11th International Symposium on Turbulence and Shear Flow Phenomena (TSFP11)*, 08 2019.